


Neutrino flavor conversion, advection, and collisions: Toward the full solution

Shashank Shalgar[✉] and Irene Tamborra[✉]

*Niels Bohr International Academy and DARK, Niels Bohr Institute, University of Copenhagen,
Blegdamsvej 17, 2100 Copenhagen, Denmark*

 (Received 13 July 2022; revised 22 February 2023; accepted 6 March 2023; published 23 March 2023)

At high densities in compact astrophysical sources, the coherent forward scattering of neutrinos onto each other is responsible for making the flavor evolution nonlinear. Under the assumption of spherical symmetry, we present the first simulations tracking flavor transformation in the presence of neutrino-neutrino forward scattering, neutral and charged current collisions with the matter background, as well as neutrino advection. We find that, although flavor equipartition could be one of the solutions, it is not a generic outcome, as often postulated in the literature. Intriguingly, the strong interplay between flavor conversion, collisions, and advection leads to a spread of flavor conversion across the neutrino angular distributions and neighboring spatial regions. Our simulations show that slow and fast flavor transformation can occur simultaneously. In the light of this, looking for crossings in the electron neutrino lepton number as a diagnostic tool of the occurrence of flavor transformation in the high-density regime is a limiting method.

DOI: [10.1103/PhysRevD.107.063025](https://doi.org/10.1103/PhysRevD.107.063025)

I. INTRODUCTION

In neutrino-dense sources, such as core-collapse supernovae, the large number of neutrinos drives the source physics, despite the weakness of their interaction [1–5]. Tracking the neutrino flavor evolution in the source core is a complex task because, in addition to resonant conversion of neutrinos in matter [6,7], the coherent forward scattering of neutrinos on other neutrinos makes the flavor evolution nonlinear [8–12]. Neutrino self-interaction is a peculiar phenomenon: neutrinos with different momenta undergo flavor evolution with identical characteristic frequency [13–20].

In the context of core-collapse supernovae, collective neutrino oscillation was originally conceptualized within the “neutrino-bulb” model [15]. The latter was based on the assumption of spherical symmetry and instantaneous decoupling of all neutrino flavors at a single radius. Within this framework, neutrino self-interaction leads to a swap in the energy distributions of the electron and nonelectron flavors, the spectral split [13,15,17–19,21–24]. However, soon it was realized that the nonlinear nature of neutrino collective effects leads to spontaneous breaking of symmetries [25,26].

Neutrinos of different flavors interact with matter differently. As a consequence, a crossing between the angular distributions of electron neutrinos and antineutrinos, the electron lepton number (ELN) crossing, may occur [27,28]. Because of this feature, neutrinos experience a flavor instability, also in the limit of vanishing vacuum frequency

[12,29–36]. The flavor transformations resulting from such a flavor instability can occur at arbitrarily large neutrino number densities [12,29,31,34,37–43]. The corresponding characteristic frequency associated with flavor transformation can be very large, lending the phenomenon the name of “fast flavor conversion” to distinguish it from the ordinary neutrino self-interaction [12,32]. The latter is also named “slow” collective oscillation since it is governed by a combination of the neutrino-neutrino self-interaction potential and the vacuum frequencies [10,11].

Despite being driven by the angular distributions of neutrinos, fast flavor conversion is further affected by the vacuum term and by the presence of all three neutrino flavors [37,39,41,44,45], as well as by symmetry breaking effects [46]. Moreover, collisions can enhance or suppress fast flavor transition according to the neutrino angular distributions [47–52]. Unlike in the case of the neutrino-bulb model, which ignores the temporal dependence of the neutrino field due to advection, the motion of neutrinos can alter their momentum distribution; this can, in turn, affect the flavor evolution [38,52–54].

Favorable conditions for the occurrence of fast flavor instabilities have been found in core-collapse supernovae as well as in compact binary merger remnants [27,28,42,55–70]. These developments have triggered intense research work aiming to assess the feedback of flavor transformation on the source physics. However, a deeper assessment of the extent of flavor conversion is still lacking.

This paper expands on our earlier work [52], where we have reported on the impact of fast flavor conversion on the

decoupling of neutrinos from matter in core-collapse supernovae. Our paper begins in Sec. II, where we introduce the formalism and outline the setup of our model. In Sec. III, we compute the classical steady state distribution of neutrinos in the absence of flavor transformation. First, we explore how the angular distributions of neutrinos evolve as functions of the radius and become forward peaked as neutrinos decouple from matter. Then, for illustrative purposes, we carry out the linear stability analysis restricting ourselves to the homogenous mode and by relying on the classical steady state distributions. Section IV focuses on the nonlinear regime of flavor conversion in the presence of neutrino-neutrino interaction, advection, and collisions with the matter background. Finally, we discuss and summarize our findings in Sec. V. Appendix provides additional details on the numerical convergence of the simulations.

II. PROBLEM SETUP

In this section, we introduce the neutrino equations of motion. Then, we provide details on the simulation setup and the parameters adopted to model the neutrino flavor evolution.

A. Neutrino equations of motion

For the sake of simplicity, we assume that neutrinos are monoenergetic and work in the two flavor (ν_e, ν_x) approximation. However, note that additional modifications to the flavor conversion physics may be derived by relaxing such approximations [37,39,44,45].

The evolution of flavor can be investigated in terms of Wigner transformed 2×2 density matrices in the flavor space for neutrinos and antineutrinos, $\rho(r, \cos \theta, t)$ and $\bar{\rho}(r, \cos \theta, t)$, respectively. The diagonal elements of the density matrix, ρ_{ii} (with $i = e, x$), stand for the occupation numbers of neutrinos of different species, while the off-diagonal terms ρ_{ij} encode flavor coherence. As shown in Fig. 1, the parameter r represents the radial direction, while $\theta \equiv \theta(r)$ is the angle with respect to the radial direction at the given r , which should not be confused with the emission angle. The time variable is represented by t .

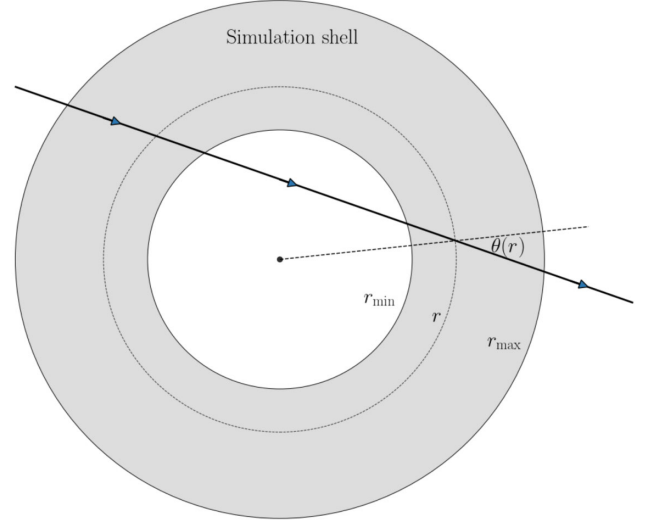


FIG. 1. Schematic diagram of our simulation shell. The gray shell illustrates the geometry of the region in which the simulation is carried out from r_{\min} to r_{\max} . The dotted line shows the radial direction, while the solid line represents a straight neutrino trajectory. Neutrinos can be emitted, absorbed, or undergo direction changing interactions along any trajectory. For any given trajectory, the angle with respect to the radial direction $[\theta(r)]$ depends on the radius. Note that, because of spherical symmetry, the neutrino angular distributions are identical irrespective of the orientation of the radial direction for all flavors.

The equations of motion that determine the flavor evolution of neutrinos and antineutrinos are given by [71]:

$$i \left(\frac{\partial}{\partial t} + \vec{v} \cdot \nabla \right) \rho(r, \cos \theta, t) = [H, \rho(r, \cos \theta, t)] + i\mathcal{C} \quad (1)$$

$$i \left(\frac{\partial}{\partial t} + \vec{v} \cdot \nabla \right) \bar{\rho}(r, \cos \theta, t) = [\bar{H}, \bar{\rho}(r, \cos \theta, t)] + i\bar{\mathcal{C}}. \quad (2)$$

The left-hand sides of Eqs. (1) and (2) contain the total derivative, including the advective term. Due to the radial dependence of θ and the assumption of spherical symmetry, the advective term can be written as follows [72]:

$$\begin{aligned} \vec{v} \cdot \nabla \rho(r, \cos \theta, t) &= \cos \theta \frac{d}{dr} \rho(r, \cos \theta, t) \\ &= \cos \theta \frac{\partial \rho(r, \cos \theta, t)}{\partial \cos \theta} \frac{d \cos \theta}{dr} + \cos \theta \frac{\partial \rho(r, \cos \theta, t)}{\partial r} \\ &= \frac{\partial \rho(r, \cos \theta, t)}{\partial \cos \theta} \frac{\sin^2 \theta}{r} + \cos \theta \frac{\partial \rho(r, \cos \theta, t)}{\partial r}. \end{aligned} \quad (3)$$

The right-hand sides of Eqs. (1) and (2) consist of the Hamiltonian that governs the flavor evolution and the collision term. The Hamiltonian includes the vacuum and self-interaction terms:

$$H = H_{\text{vac}} + H_{\nu\nu}, \quad (4)$$

with

$$H_{\text{vac}} = \frac{\omega}{2} \begin{pmatrix} -\cos 2\vartheta_V & \sin 2\vartheta_V \\ \sin 2\vartheta_V & \cos 2\vartheta_V \end{pmatrix} \quad (5)$$

$$H_{\nu\nu} = \mu_0 \int [\rho(\cos \theta') - \bar{\rho}(\cos \theta')] \times (1 - \cos \theta \cos \theta') d \cos \theta'. \quad (6)$$

We use ϑ_V to denote the vacuum mixing angle, while $\omega = \Delta m^2/2E$ is the vacuum frequency with E being the neutrino energy. In the self-interaction Hamiltonian, $H_{\nu\nu}$, μ_0 denotes the self-interaction strength. The additional integration over the azimuthal angle in Eq. (6) results in a factor 2π , which has been absorbed in μ_0 . Note that, due to the radial evolution of the angular distributions of neutrinos, the effective self-interaction strength decreases as a function of the radius in the regions beyond the neutrinosphere. The Hamiltonian governing the evolution of antineutrinos is the same as Eq. (4), with $H_{\text{vac}} \rightarrow -H_{\text{vac}}$. The matter term in the Hamiltonian is neglected since its effect is to reduce the effective mixing angle of neutrinos [73].

The collision term includes emission, absorption, and direction-changing collisions, respectively [74], i.e., it takes into account the main reactions of neutrinos with the matter background [27,75–78]. This implies $\mathcal{C} \equiv \mathcal{C}(\vec{r}, E, t) = \mathcal{C}_{\text{emission}} + \mathcal{C}_{\text{absorb}} + \mathcal{C}_{\text{dir-ch}}$:

$$\mathcal{C}_{\text{emission}}^{\nu_e, \bar{\nu}_e, \nu_x, \bar{\nu}_x} = \frac{1}{\lambda_{\text{emission}}^{\nu_e, \bar{\nu}_e, \nu_x, \bar{\nu}_x}(r)}, \quad (7)$$

$$\mathcal{C}_{\text{absorb}}^{\nu_e, \bar{\nu}_e, \nu_x, \bar{\nu}_x} = -\frac{1}{\lambda_{\text{absorb}}^{\nu_e, \bar{\nu}_e, \nu_x, \bar{\nu}_x}(r)} \rho_{ii}(\cos \theta), \quad (8)$$

$$\mathcal{C}_{\text{dir-ch}}^{\nu_e, \bar{\nu}_e, \nu_x, \bar{\nu}_x} = -\frac{2}{\lambda_{\text{dir-ch}}^{\nu_e, \bar{\nu}_e, \nu_x, \bar{\nu}_x}(r)} \rho_{ii}(\cos \theta) + \int_{-1}^1 \frac{1}{\lambda_{\text{dir-ch}}^{\nu_e, \bar{\nu}_e, \nu_x, \bar{\nu}_x}(r)} \rho_{ii}(\cos \theta') d \cos \theta'. \quad (9)$$

Each of the above equations refers to all flavors as denoted by the superscripts. In principle, $\mathcal{C} \equiv \mathcal{C}(r, \cos \theta, E, t)$ and

the ratio among the different terms entering the collision term changes as a function of energy and time [75–78]. However, for the sake of simplicity, we omit any dependence on E and t . In addition, due to the small timescales associated with fast flavor evolution compared to the collision term, the off-diagonal components do not play any significant role (we have numerically verified that this assumption holds; results not shown here). We also neglect the Pauli blocking and neutrino chemical potentials for the sake of simplicity, although they should be taken into account once more an advanced modeling of the collision term is developed [79,80].

B. Simulation setup

We carry out the simulations presented in this paper in a “simulation shell,” see gray shaded region in Fig. 1. The radial range extends from $r_{\text{min}} = 15$ km to $r_{\text{max}} = 30$ km, while $\cos \theta(r) \in [-1, 1]$ at each r . We use a grid of 150 uniform bins for both $\cos \theta$ and r . We have tested the convergence of the code with respect to the number of bins and provide further details in the Appendix. We use $E = 20$ MeV $\Delta m^2 = 2.5 \times 10^{-3}$ eV², $\mu_0 = 10^4$ km⁻¹, and the effective vacuum mixing angle $\vartheta_V = 10^{-3}$.

At $r = r_{\text{min}}$, the boundary condition is determined by the collision term. At $r = r_{\text{max}}$, we impose two different boundary conditions depending on $\cos \theta$. For $\cos \theta > 0$, neutrinos stream outward and, hence, the boundary condition is determined by conditions within the simulation region. For $\cos \theta \leq 0$, we impose a vanishing boundary condition.

In order to investigate the dependence of fast flavor conversion on the shape of the ELN crossings, we consider three different collision terms: Cases A, B, and C, engineered to give different types of ELN crossings. Case A is also adopted in Ref. [52]. The flavor-dependent length-scales entering the collision terms in Eqs. (7)–(9) are reported in Table I. For all collision terms, we use a simplified radial dependence defined by $\lambda_{\text{emission, absorb, dir-ch}}^{\nu_i} \sim 1/\xi(r)$, with $\xi(r) = \exp(15 - r/\text{km})$. We refer the reader to Appendix of Ref. [52] for further details on the modeling of our heuristic collision term. We parametrize \mathcal{C} to have a characteristic length scale of $\mathcal{O}(10\text{--}100)$ m at r_{min} for all cases and so that \mathcal{C} falls

TABLE I. Length scales associated with emission, absorption, and direction changing scattering for Cases A, B, and C. The collision terms for ν_e and ν_x are identical for all cases, but they differ from each other for $\bar{\nu}_e$. The function $\xi(r)$ is used to represent the function $\exp(15 - r)$. All the collision terms are in units for km⁻¹ and r is in km.

	ν_e (Cases A, B, C)	$\bar{\nu}_e$ (Case A)	$\bar{\nu}_e$ (Case B)	$\bar{\nu}_e$ (Case C)	$\nu_x, \bar{\nu}_x$ (Cases A, B, C)
$\lambda_{\text{emission}}^{\nu_i}$ (km)	$1/[50 \xi(r)]$	$1/[50 \xi(r)]$	$1/[26 \xi(r)]$	$1/[30 \xi(r)]$	$1/[10 \xi(r)]$
$\lambda_{\text{absorb}}^{\nu_i}$ (km)	$1/[50 \xi(r)]$	$1/[50 \xi(r)]$	$1/[25 \xi(r)]$	$1/[25 \xi(r)]$	$1/[10 \xi(r)]$
$\lambda_{\text{dir-ch}}^{\nu_i}$ (km)	$1/[50 \xi(r)]$	$1/[25 \xi(r)]$	$1/[25 \xi(r)]$	$1/[25 \xi(r)]$	$1/[12.5 \xi(r)]$

exponentially as a function of r . We stress that this is a simplification, not aiming to reproduce realistic conditions in the supernova core, but rather allowing to pass from isotropic to forward peaked distribution within the simulation shell and to generate an ELN crossing, as discussed in the next section. Since we populate the simulation shell through collisions, the collisions term for ν_e in Table I is chosen such that r_{\min} is within the trapping region and the neutrino number density there is governed only by the ratio of $\mathcal{C}_{\text{emission}}$ and $\mathcal{C}_{\text{absorb}}$.

The collision term involves factors that give rise to exponentially growing and damping solutions, which make them stiff. We use the Adams–Bashforth–Moulton method from the `Differentialequations.jl` package of Julia to solve the equations of motion [81,82]. Each simulation took $\mathcal{O}(2000)$ CPU hours employing shared memory on the High Performance Computing Centre at the University of Copenhagen.

III. CLASSICAL STEADY STATE CONFIGURATION: NO FLAVOR CONVERSION

In this section, we present our results on the classical steady state configuration achieved in the absence of flavor conversion. On the basis of these findings, we then introduce the linear stability analysis to investigate the regions in the simulation shell where the development of flavor instabilities is foreseen.

A. Angular distributions of neutrinos

In the absence of flavor conversion (i.e., $H = \bar{H} = 0$ in Eqs. 1 and 2), we aim to find a classical steady state configuration by setting $\rho_{ij} = 0$ as the initial condition for all flavors (the off-diagonal terms of the density matrices ρ_{ij} are initially equal to zero and remain as such throughout the evolution in the absence of flavor transformation) and by considering the collision and advection terms only.

Neutrinos in our setup are generated through collisions and advected across the simulation shell. The advective term allows for a change in the number density of neutrinos at a given location due to their motion. As for the collision term, the emission term is independent of the number density of neutrinos, the absorption term is proportional to the number density of neutrinos, while the direction changing term conserves the number of neutrinos. To obtain the steady state configuration, we need to evolve the neutrino field in our simulation shell at least for a period corresponding to the radial range $[r_{\min}, r_{\max}]$, assuming that neutrinos travel at the speed of light, i.e., $t = 5 \times 10^{-5}$ s. In the simulations, we have evolved the system for $t = 10^{-4}$ s out of caution.

The top panel of Fig. 2 shows a polar diagram of the angular distribution of ν_e for Case C, which we consider our benchmark configuration hereafter, once the steady state configuration is achieved. We obtain an isotropic

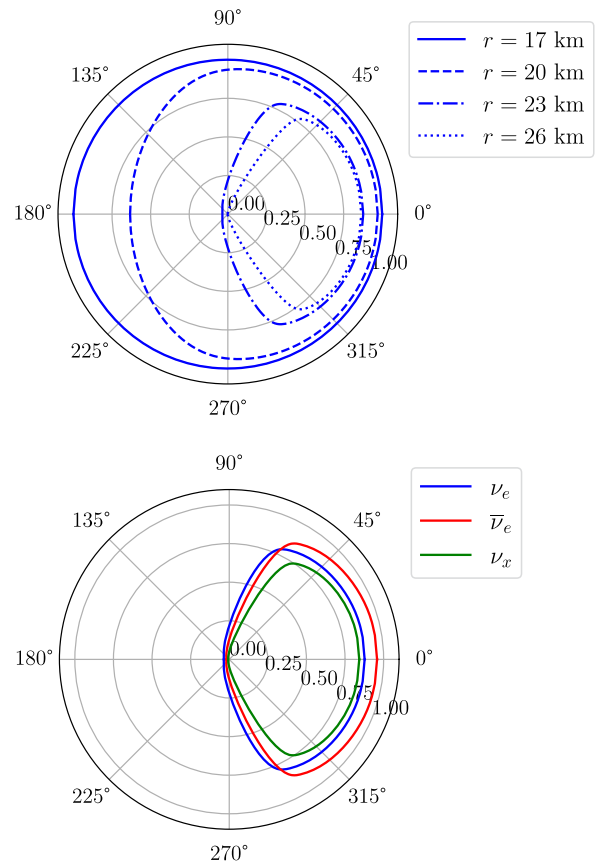


FIG. 2. Top: Polar diagram of the steady state angular distribution of ν_e for different radii for Case C in the absence of neutrino transformation. The angle $\theta = 0$ corresponds to the local radial direction. At small radii the angular distribution is isotropic and slowly becomes forward peaked with falling matter density. Bottom: Polar diagram of the angular distributions of ν_e , $\bar{\nu}_e$ and ν_x at $r = 23$ km. Because of the different interaction rates with matter, the distributions of neutrinos of different flavors are not equally forward peaked, with the angular spread being the largest for ν_e , followed by $\bar{\nu}_e$ and ν_x .

configuration at small radii, which slowly becomes forward peaked at larger radii as the density falls. Such a trend holds for all flavors. However, as we move toward larger radii and the density falls, ν_x start forward peaking, followed by $\bar{\nu}_e$ and ν_e , as displayed in the bottom panel of Fig. 2. This behavior can lead to ELN crossings and hence fast flavor instabilities. The qualitative trend in the angular distributions for Cases A and B is similar to the one of Case C and therefore not shown here.

The classical steady state obtained as described above constitutes the initial configuration adopted to solve the neutrino equations of motion including flavor conversion (see Sec. IV). This procedure is important from a numerical point of view. Any configuration that is not initially in a classical steady state leads to large gradients at the edges of the simulation shell, which give rise to numerical instabilities. Moreover, the advective term involves the

calculation of the derivatives using a finite-element method, leading to numerical instabilities without sufficient resolution. Various tests have been carried out to make sure that numerical instabilities do not affect the results presented here.

B. Looking for flavor instabilities through the classical steady state solutions

It has been proven that the existence of ELN crossings is a necessary condition for fast flavor instabilities [34,83]. In order to gauge the presence of ELN crossings, we rely on a slightly modified definition of the ζ parameter introduced in Ref. [84] and evaluate it at the time when the steady state configuration has been reached:

$$\zeta(r) = \mu_0 \frac{I_1(r)I_2(r)}{I_1(r) + I_2(r)}, \quad (10)$$

with

$$I_1(r) = \int [\rho_{ee}(r, \cos \theta) - \bar{\rho}_{ee}(r, \cos \theta)] d \cos \theta \quad (11)$$

for $\rho_{ee}(r, \cos \theta) > \bar{\rho}_{ee}(r, \cos \theta)$ and

$$I_2(r) = \int [\bar{\rho}_{ee}(r, \cos \theta) - \rho_{ee}(r, \cos \theta)] d \cos \theta \quad (12)$$

for $\rho_{ee}(r, \cos \theta) < \bar{\rho}_{ee}(r, \cos \theta)$. The ζ parameter can be different from zero if and only if there are regions in the angular domain where $\rho_{ee}(\cos \theta) > \bar{\rho}_{ee}(\cos \theta)$ and other regions in the angular domain where $\rho_{ee}(\cos \theta) < \bar{\rho}_{ee}(\cos \theta)$, which implies the existence of an ELN crossing. Figure 3 shows the radial profile of ζ for Cases A, B, and C. An ELN crossing exists for $r \gtrsim 18$ km for all cases; hence one should expect a potential flavor instability in this region.

To better gauge which regions of the simulation shell may be prone to flavor instabilities, we rely on the linear stability analysis of the classical steady state solution obtained in Sec. III A for Cases A, B, and C (see Table I). In particular, we focus on flavor instabilities in the limit of vanishing and nonvanishing vacuum frequency (i.e., fast and slow flavor instabilities). For the sake of simplicity, we focus on the linear stability analysis for the homogeneous mode only, since we aim to gain insight on where flavor conversion may develop. This simplifying choice is also justified by the fact that if the neutrino gas is not homogeneous, as in our case, the equations for the Fourier modes are coupled. Note, however, that the numerical results presented in Sec. IV do not distinguish between homogeneous and inhomogeneous modes and do take into account collisions and advection.

To this purpose, we linearize Eqs. (1) and (2) ignoring the collision and advective terms. The linearization implies

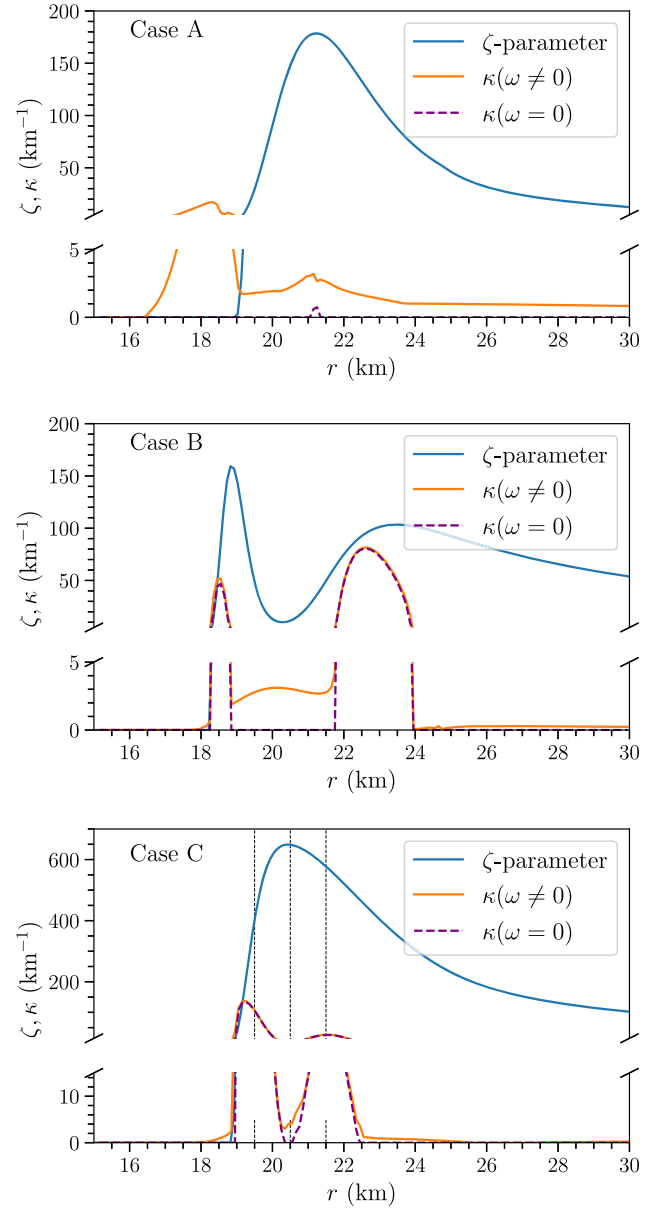


FIG. 3. Radial profiles of the ζ parameter (see Eq. (10); solid blue line) and growth rates calculated for the homogeneous mode using the linear stability analysis for the cases of vanishing (dashed magenta line) and nonvanishing (solid orange line) vacuum frequency for Cases A, B, and C from top to bottom, respectively. The nonzero ζ -parameter implies the existence of an ELN crossing, which is a necessary condition for the existence of fast flavor instability. In all three cases, the ζ parameter peaks where the $\omega = 0$ flavor instability occurs. Moreover, there are radii for which a flavor instability exists only for $\omega \neq 0$. A broken y-axis is adopted because of the significant difference in the growth rates of the instability for the fast ($\omega = 0$) and the slow ($\omega \neq 0$) cases. The difference between the orange solid line and the purple dashed line highlights the impact of the vacuum frequency on the growth rate. For radii where the fast growth rate is substantial, the vacuum term has negligible effect. But when the fast growth rate is small or absent the vacuum term can become important. The dashed vertical lines in the bottom panel denote the radii at which the absolute values of the components of the eigenvectors are shown in Fig. 4.

expanding the equations of motion for the off-diagonal components of the density matrix $\rho_{\text{ex}}(r, \cos \theta, t)$ up to linear order in $\rho_{\text{ex}}(r, \cos \theta, t)$ [and the same for $\bar{\rho}_{\text{ex}}(r, \cos \theta, t)$] [34,85]. For each r , the results are solutions for $\rho_{\text{ex}}(r, \cos \theta, t)$ and $\bar{\rho}_{\text{ex}}(r, \cos \theta, t)$ of the form:

$$\rho_{\text{ex}}(r, \cos \theta, t) \sim \exp(-i\Omega t)\rho_{\text{ex}}(r, \cos \theta, 0), \quad (13)$$

$$\bar{\rho}_{\text{ex}}(r, \cos \theta, t) \sim \exp(-i\Omega t)\bar{\rho}_{\text{ex}}(r, \cos \theta, 0), \quad (14)$$

where Ω is the eigenvalue which is independent of $\cos \theta$ and it is the same for neutrinos and antineutrinos, due to the collective nature of the flavor evolution. The eigenvalue Ω can be obtained semianalytically and either is real or appears in complex-conjugate pairs. A complex Ω with a nonzero imaginary part κ implies that ρ_{ex} and $\bar{\rho}_{\text{ex}}$ grow exponentially; this is known as flavor instability [85].

The flavor instability thus obtained can be classified as a “fast” flavor instability, if it exists in the limit $\omega \rightarrow 0$, and “slow” flavor instability otherwise. Note that this definition of slow flavor instability is a generalization of the one commonly adopted in the literature, invoking the existence of at least one crossing between the electron and nonelectron flavors either in energy [17–19,21,86] or in angle [87,88]. The crossing would determine the development of a flavor instability while conserving the lepton number. As discussed later, the presence of ELN crossings (in angle) for our system of monoenergetic neutrinos is enough to guarantee the development of slow flavor instabilities for $\omega \neq 0$. The presence of a fast flavor instability requires that an ELN crossing occurs, which means that there is at least one angle for which $\rho_{ee}(\cos \theta) = \bar{\rho}_{ee}(\cos \theta)$. On the other hand, the presence of an ELN crossing does not necessarily imply the existence of a flavor instability or large flavor conversion [84,89].

Figure 3 shows the growth rate of the flavor instability obtained by relying on the linear stability analysis. A nonzero value of the growth rate κ denotes the regions of flavor instability for $\omega = 0$ and $\omega \neq 0$, and in the absence of advection and collisions. One can see that the ζ parameter peaks in the same region where the flavor instability for $\omega = 0$ is most prominent, confirming that the ζ parameter is a good indicator of the regions of instability [84].

Figure 3 displays a substantial radial range where the flavor instability is present for all cases. However, not all regions that exhibit a flavor instability do so due to a fast flavor instability. In some radial regions, the flavor instability is due to slow collective modes, as can be seen by comparing the orange curve with the magenta one. Moreover, for Cases B and C, the growth rates for $\omega = 0$ and $\omega \neq 0$ coincide for some spatial regions. The growth rate for the fast flavor instability is much faster than the one of the slow flavor instability for the homogeneous

mode, as seen by comparing the radial range for which only the slow flavor instability is present in Fig. 3 with the one where the fast instability occurs.

The fact that there are regions where the fast instabilities occur with the growth rate being strongly influenced by the vacuum term demands for a reassessment of the distinction between fast and slow flavor instabilities. In fact, the presence of a slow flavor instability near the decoupling region has not been shown in the literature before, because most studies do not follow the evolution of the angular distributions as functions of the radius or they just focus on one of the two instabilities ($\omega = 0$ or $\omega \neq 0$). The implications of the presence of slow flavor instabilities near the decoupling region could show many more interesting results in multi-energy calculations because of the large vacuum frequency associated with the low energy tail

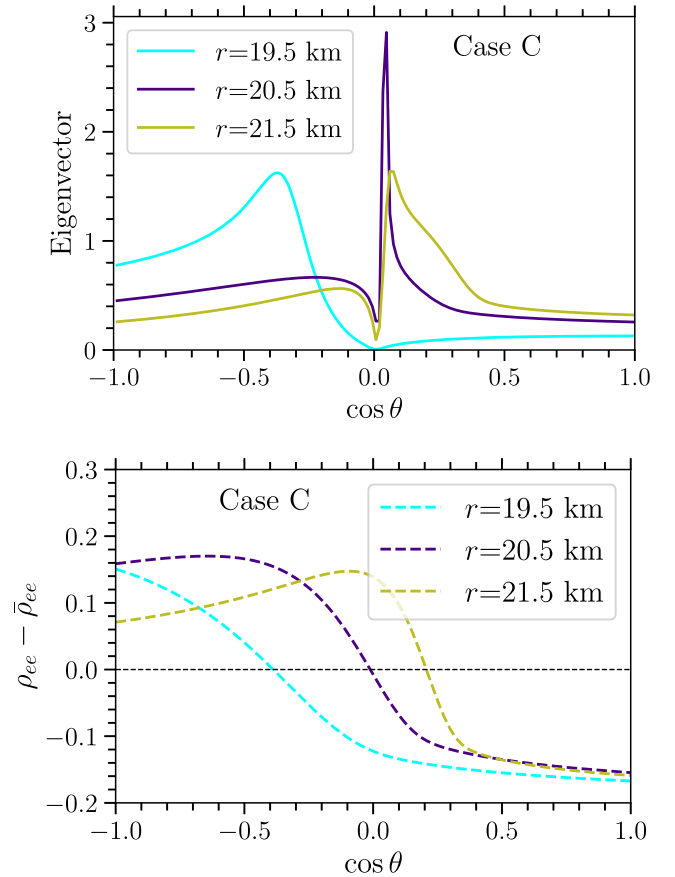


FIG. 4. Top: Absolute value of the components of the eigenvectors as functions of $\cos \theta$ for Case C at 19.5, 20.5, and 21.5 km in cyan, indigo, and olive, respectively. The eigenvector components are normalized such that their integral over $\cos \theta$ is 1. The radii at which the eigenvectors are computed are marked by vertical lines in the bottom panel of Fig. 3. Bottom: Difference between the angular distributions of ν_e and $\bar{\nu}_e$ in the absence of flavor transformation (i.e., ELN angular distribution) for the same radii as in the top panel. The eigenvector peaks in the region of the ELN crossing.

of the neutrino distributions and its interplay with fast modes [10,11,37].

For both slow and fast instabilities, the absolute value of the eigenvectors determines the angular regions where flavor transformation first manifests itself for the homogeneous mode. Comparing the top and bottom panels of Fig. 4, we can see that the absolute value of the eigenvector for Case C peaks near the region of the ELN crossing (see also the bottom panel of Fig. 3 where the ζ parameter peaks). It is also interesting to note that the absolute value of the eigenvector is zero or nearly zero in the proximity of $\cos\theta = 0$ (see Fig. 4). This divides the angular regions in two distinct regions which show qualitatively different flavor evolution, and flavor transformation in one domain ($\cos\theta \in [0, 1]$) does not easily spread to the other domain ($\cos\theta \in [-1, 0]$), as discussed in Sec. IV. From Fig. 3, we conclude that we should expect fast instabilities for $r = 19.5$ and 21.5 km, and slow instability for $r = 20.5$ km. Interestingly, we can see from Fig. 4 that the slow instability for $r = 20.5$ km still develops in the proximity of the ELN crossing, generalizing the findings of Refs. [87,88].

IV. QUASISTEADY STATE CONFIGURATION: FLAVOR CONVERSION PHYSICS

In this section, we investigate the quasisteady state configuration reached by our system in the presence of flavor transformation. We then explore the effects of flavor conversion on neutrino decoupling, expanding on the findings of Ref. [52], before to discuss the dynamical coupling among flavor conversion, collisions, and neutrino advection.

A. Neutrino flavor transformation in the nonlinear regime

In the presence of flavor conversion, this paper aims to find a “quasisteady state” solution of Eqs. (1) and (2). In fact, due to the nonlinear nature of the flavor evolution, it is not possible to obtain a flavor configuration for which the neutrino flavor remains constant as a function of time for each $\cos\theta$ and r . The spatial and angular structures continue to evolve on smaller and smaller scales. The quasisteady state configuration should be reached by solving Eqs. (1) and (2) irrespective of the initial condition. However, from a numerical perspective, it is convenient to start with a configuration that is as close to the classical steady state configuration as possible.

Figure 5 shows a contour plot of the difference between ρ_{ee} with and without neutrino mixing in the plane spanned by $\cos\theta$ and r for Cases A, B, and C. The density matrix element, ρ_{ee}^{mix} was calculated by using the classical steady state configuration ($\rho_{ee}^{\text{no-mix}}$) as the initial condition. The latter was then evolved up to 5×10^{-5} s, which corresponds to the size of the simulation shell divided by the

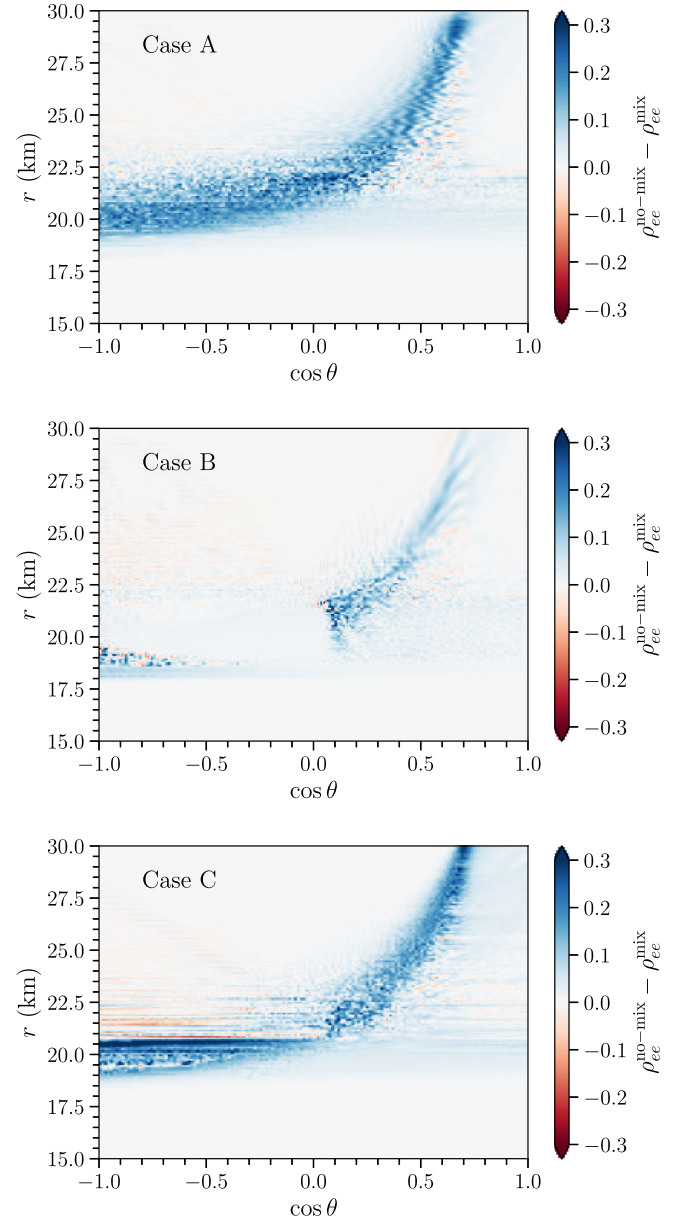


FIG. 5. Contour plot of the difference between ρ_{ee} with and without neutrino mixing, in the presence of collisions and advection in the plane spanned by $\cos\theta$ and r for Cases A, B, and C, from top to bottom respectively. Red parts show the regions in the parameter space for which there are less electron neutrinos due neutrino flavor transformation with respect to the case without neutrino mixing, while the opposite is true for the blue regions. A similar trend occurs for $\bar{\nu}_e$ and it is not shown here.

speed of light. If a smaller value of mixing angle is used, it takes longer for the system to reach the quasi steady state, but the results are unchanged.

By comparing with Figs. 5 and 3 and by taking into account the findings of Refs. [52,89], we conclude that looking for flavor instabilities is not enough to predict the radial regions actually affected by flavor conversion. In

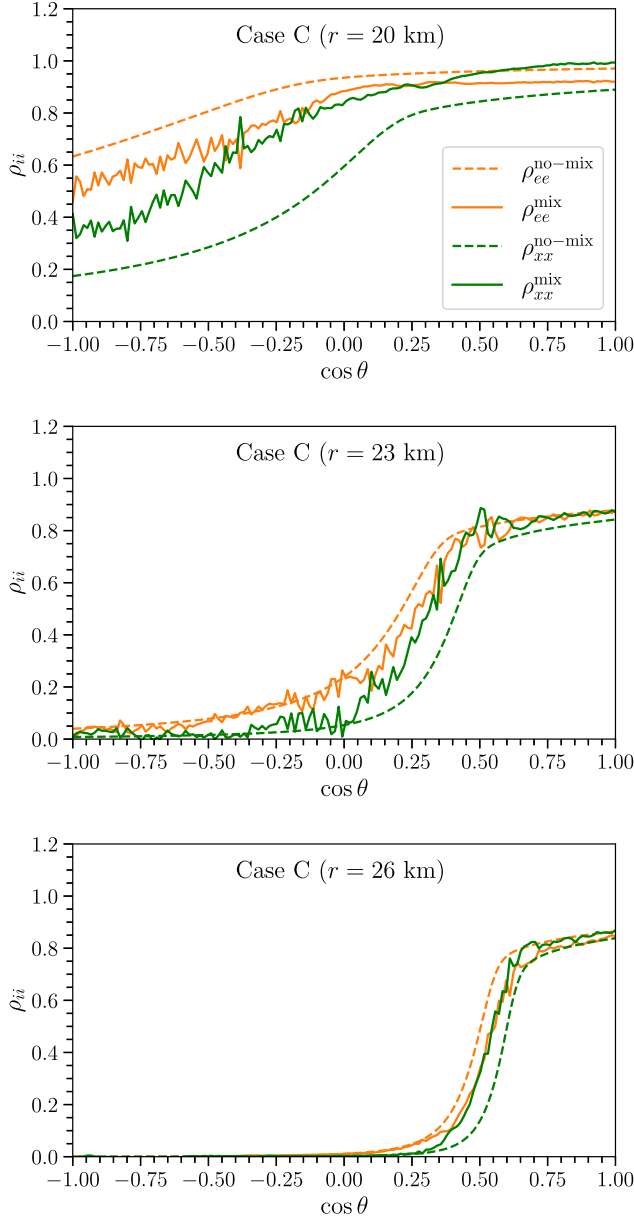


FIG. 6. Angular distributions of ρ_{ee} (in orange) and ρ_{xx} (in green) for Case C at 20, 23, and 26 km, from top to bottom, respectively. The dashed lines show the angular distributions in the absence of neutrino mixing while the solid lines show the same with neutrino mixing. Flavor transformation affects an angular range larger than the one where the ELN crossing is initially present.

fact, the neutrinos that undergo flavor transformation at one radius are transported to larger radii due to advection. Cases B and C show an interesting phenomenology for the effect of advection and collisions, since the flavor instability is limited to a small range of the radial region (Fig. 3), but the actual region affected by flavor conversion is larger because of the dynamical effects induced by advection and collisions (Fig. 5).

The results from the numerical simulations show a spread in the flavor transformation to a finite domain of angular range, typically on one side of the ELN crossing as visible by comparing Figs. 3 and 6. To some extent, the essence of this phenomenon is captured in a homogeneous system with collisions [12,47]. From Fig. 6, we can also see that, as r increases, the angular distributions become more forward peaked and the distributions of ν_e and ν_x are similar to each other. As a consequence, the angular distributions after flavor transformation of ν_e and ν_x tend to be similar to each other for certain r , however, this does not imply that flavor equipartition is a general finding.

The spread of flavor transformed neutrinos from one radius to another is visible in the angle averaged neutrino occupation number as a function of the radius. We define the (quasi) steady state angle averaged neutrino number density as follows:

$$\langle \rho_{ii}(r) \rangle = \frac{\int \rho_{ii}(r, \cos \theta) d \cos \theta}{\int d \cos \theta}. \quad (15)$$

Figure 7 shows the radial profiles of $\langle \rho_{ii}(r) \rangle$ for Cases A, B, and C. Note that in the absence of advection and collisions, unitary evolution dictates that $\langle \rho_{ee}^{\text{mix}} \rangle$ lies in between $\langle \rho_{ee}^{\text{no-mix}} \rangle$ and $\langle \rho_{xx}^{\text{no-mix}} \rangle$ for all radii. However, due to the presence of advection and collision, Fig. 7 shows that this no longer holds; see for example Case B at $r \simeq 18$ km.

It is worth stressing that it is not possible to disentangle the effects of collisions and advection in our formalism. Nevertheless, their interplay ensures that neutrinos see different angular distributions over the simulation time, thus capturing the essence of the effects highlighted in Refs. [47,84].

B. Effects of flavor transformation on neutrino decoupling

As discussed in Ref. [52], the angle averaged number density of neutrinos of various flavors offers insight into the effect of flavor transformation on neutrino decoupling. In order to predict the region where decoupling approximately occurs, we consider the radius at which the flux factor for ν_i at the time when the quasisteady state configuration is reached,

$$\mathcal{F}_{\nu_i}(r) = \frac{\int_{-1}^1 \rho_{ii}(r, \cos \theta) \cos \theta d \cos \theta}{\int_{-1}^1 \rho_{ii}(r, \cos \theta) d \cos \theta} \simeq \frac{1}{3}. \quad (16)$$

We use this as an indicator of the effective decoupling radius since, in the coupled region, the neutrino angular distribution is isotropic, and the numerator vanishes. In the completely decoupled region, neutrinos are forward peaked and $\cos \theta \simeq 1$ for all neutrinos; hence the flux factor is thus equal to unity.

Figure 7 shows the region where $\mathcal{F}_{\nu_i}(r, t) = 1/3$ for Cases A, B, and C, generalizing the findings of Ref. [52].

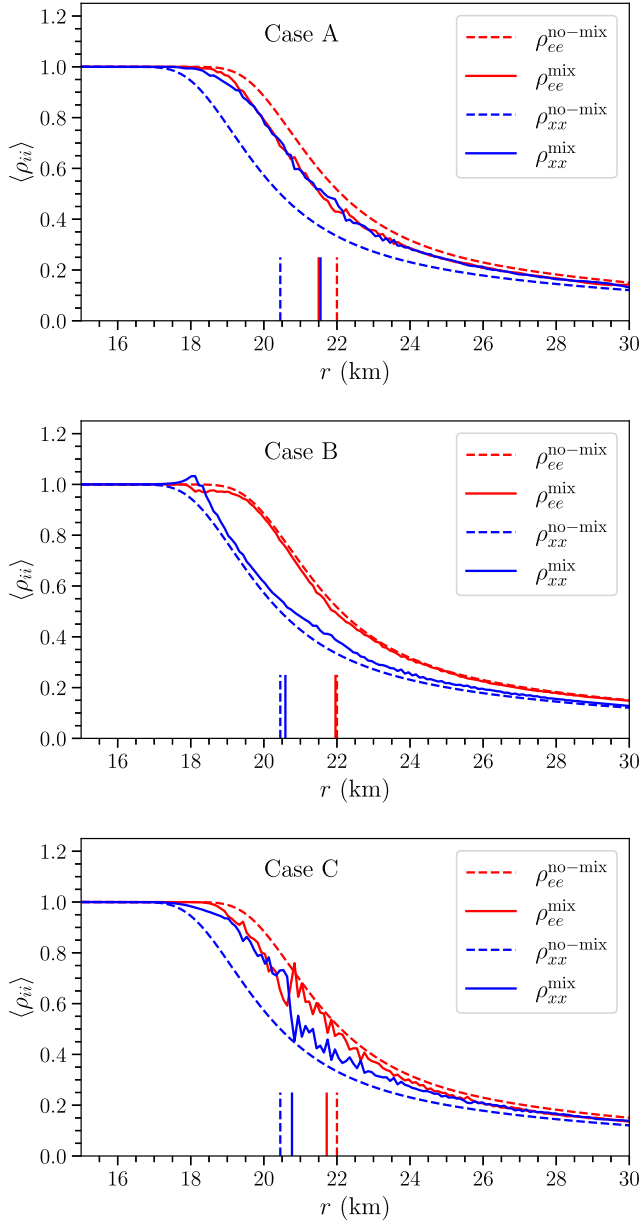


FIG. 7. Radial profile of the steady state angle-averaged ρ_{ee} (in red) and ρ_{xx} (in blue) in the presence of advection and collisions for Cases A, B, and C from top to bottom respectively. The dashed lines show the angle averaged number densities in the absence of neutrino flavor transformation, while the solid lines show the same with neutrino flavor transformation. The vertical lines mark the smallest radius at which the condition in Eq. (16) is fulfilled. While flavor equipartition is achieved in Case A, flavor equipartition is not reached in Cases B and C. In all cases, the neutrino decoupling surfaces are affected by flavor conversion according to the strength of the collision term.

However, as visible in some panels of Fig. 7, changes in the angle averaged neutrino occupation number are not always directly correlated to changes in the decoupling radius. This is a consequence of the nontrivial angular distributions arising from neutrino flavor transformation.

C. Interplay among flavor transformation, collisions, and advection

The presence of collisions and advection redistributes neutrinos over the angle bins, as also found in Refs. [38,47]. In the absence of collisions and advection, flavor transformation is predominantly present in a narrow angular range around the ELN crossing. Moreover, in the regions where neutrino flavor transformation is present, the angular structure becomes progressively finer with time. Because of this, more angle bins are required as the simulation time increases, when $\omega \neq 0$ [37,40,90]. However, the growth of structure at smaller and smaller scales is suppressed due to the presence of collisions and advection (see also Appendix and Ref. [52]). This is not surprising and it is due to the fact that the collision term redistributes neutrinos across angles. More importantly, in the present case, neutrinos at different radii undergo flavor transformation at different angles at a given time. The advective term mixes the angular distribution at various radii as neutrinos travel, reducing the number of angular bins required to reach angular convergence.

The presence of flavor transformation in the angular range where ν_e and $\bar{\nu}_e$ are approximately equal is a consequence of the assumption of azimuthal symmetry. In the absence of azimuthal symmetry, the flavor transformation is not necessarily correlated to the angular region in the proximity of the ELN crossing [46].

Recent literature has speculated that flavor equipartition or depolarization may be a general outcome of fast flavor evolution [91–93]. Our findings suggest that this is not the case in our setup. Although we find equipartition in Case A, as shown in the top panel of Fig. 7, this is not true for Cases B and C. For Case A, flavor equipartition is reached because the occupation numbers of ν_e and $\bar{\nu}_e$ are very similar in the classical steady state configuration. It is also important to note that this finding in our simulation setup is also linked to the fact that the lepton number in the neutrino sector is not conserved in our simulations due to absorption and emission collisional terms.

V. CONCLUSIONS

Understanding the evolution of neutrino flavor in dense media remains an active subject of research. In this work, expanding on Ref. [52], we investigate the flavor evolution for three different parametrizations of the collision term, consistently treating collision, advection, and flavor transformation. We rely on a spherically symmetric simulation shell and assume that all neutrinos have the same energy for simplicity. We populate the simulation shell through collisions and in the absence of flavor conversion, a steady state configuration is reached. In the presence of flavor transformation, flavor mixing spreads across angular and radial regions because of the dynamical effects induced by advection and collisions until a quasisteady state configuration is reached.

While in the literature flavor equipartition or depolarization is often presented as a general outcome of fast flavor conversion, we find that flavor equipartition is not achieved in general. Moreover, in the literature, it has been classically considered that fast flavor transformations could occur in the region of high density of neutrinos, while slow flavor collective transformations occur at larger radii and smaller densities; however, we find that an overlap between slow and fast flavor conversion could take place. This gives rise to a completely new phenomenology of neutrino self-interactions, yet to be explored.

Our work highlights the dynamical interplay among flavor conversion, advection, and collisions. In particular, we find that flavor conversion spreads across angular modes and in a larger spatial range, instead of remaining clustered in the proximity of the ELN crossing. On the other hand, the dynamical interplay among flavor conversion, advection, and collisions hinders the cascade of flavor structure to small scales, otherwise expected [37,40,90], and smears the quasisteady state distributions.

Because of the numerical challenges, our model includes some simplifications. The ones which further need to be relaxed concern the dependence on energy of flavor transformation and the collision term. In fact, fast flavor conversion is by itself not sensitive to neutrino energy, but slow flavor conversion is. Hence, a nontrivial interplay between collisions and slow flavor conversion may exist.

This work highlights the fascinating nature of neutrino self-interaction in compact astrophysical sources and the nontrivial interplay of the flavor conversion physics with neutrino advection and collisions. As such, our findings give a glimpse of flavor phenomenology that could have potentially interesting implications for the physics of compact sources and remains to be explored.

ACKNOWLEDGMENTS

We would like to thank Rasmus S.L. Hansen and Christopher Rackauckas for insightful discussions. We acknowledge support from the Villum Foundation (Project No. 13164), the Danmarks Frie Forskningsfonds (Project No. 8049-00038B), the MERAC Foundation, and the Deutsche Forschungsgemeinschaft through Sonderforschungsbereich SFB 1258 “Neutrinos and Dark Matter in Astro- and Particle Physics” (NDM).

APPENDIX: NUMERICAL CONVERGENCE

To prove numerical convergence, Fig. 8 shows the analogous of Fig. 5, but with simulations obtained by using 200×200 bins, while keeping all other inputs unchanged. One can see that the agreement between the two figures is excellent.

Naively, one might expect that the simulation radial resolution should be dictated by $1/\mu_0$ (as it would

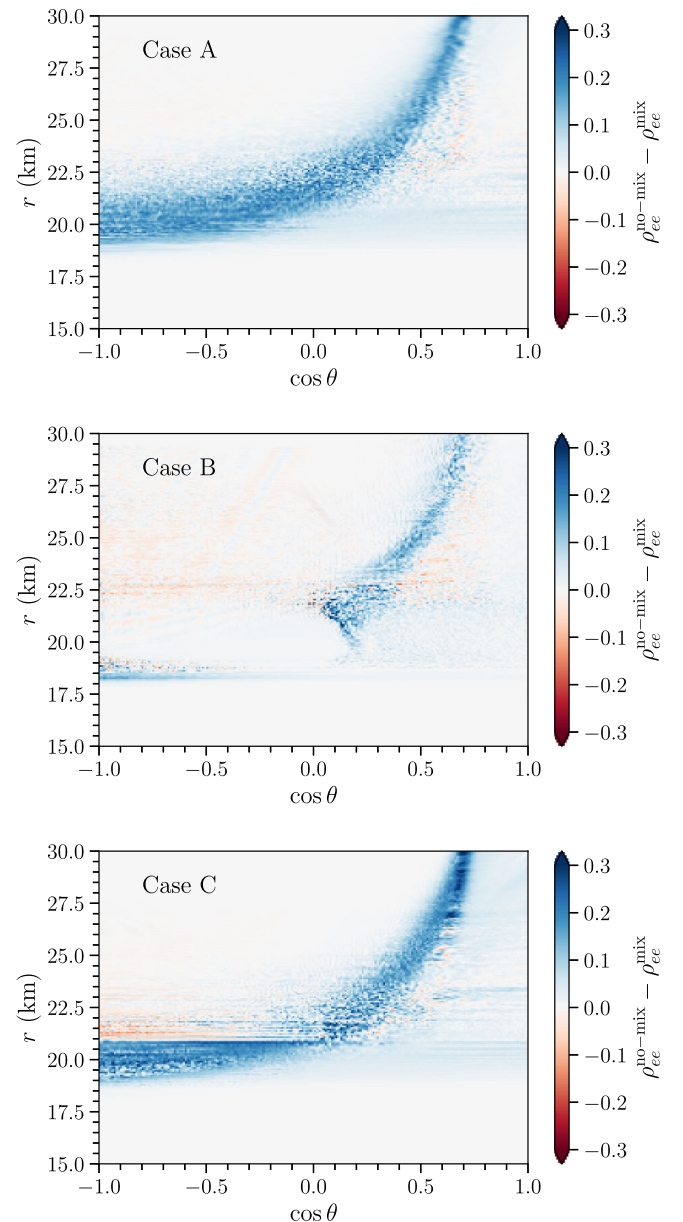


FIG. 8. Same Fig. 5, but with 200×200 bins. The results are in agreement with the ones in Fig. 5.

be the case in the absence of advection, collisions, and the vacuum term). However this is not the case in our simulation setup, because of the inclusion of neutrino advection and collisions. To this purpose, we consider two simulation sets, one with $\mu_0 = 1000 \text{ km}^{-1}$ and the other one with $\mu_0 = 100 \text{ km}^{-1}$, and for each μ_0 , we run two simulations, one with 150 and one with 1500 radial bins for Case A, while all other inputs are kept unchanged. Figure 9 shows the results: while minor differences are appreciable, the overall trend is robust. The cascade of the large scale inhomogeneous modes to small scales occurs at a rate that advection and collisions are not able to erase only for $\mu_0 = 1000 \text{ km}^{-1}$. For $\mu_0 = 100 \text{ km}^{-1}$ and 1500 radial bins,

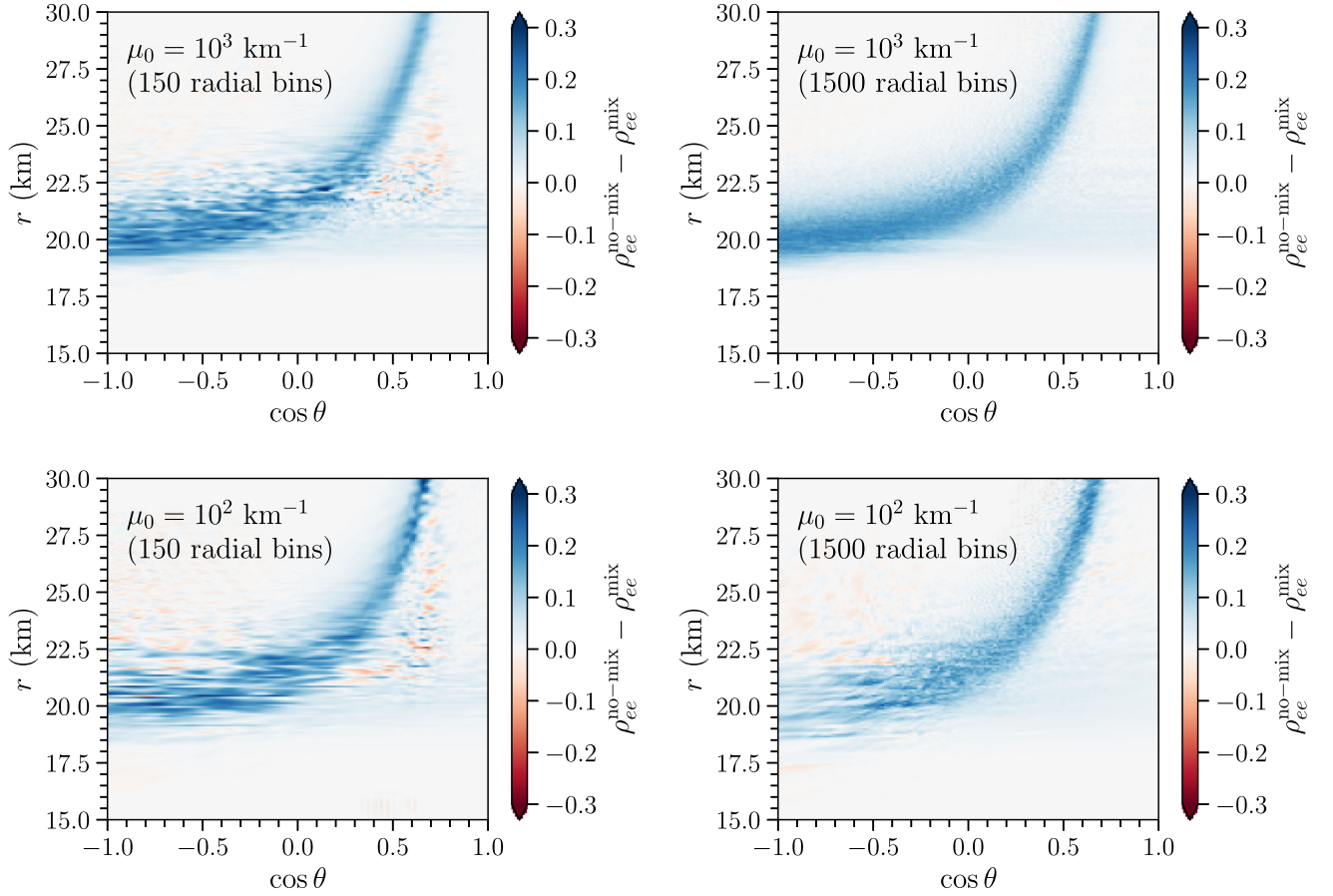


FIG. 9. Same as Fig. 5, but for Case A and $\mu_0 = 1000 \text{ km}^{-1}$ (top panels) as well as $\mu_0 = 100 \text{ km}^{-1}$ (bottom panels), with 150 (left) and 1500 (right) radial bins. The average relative error between the simulations with different number of radial bins is 1.16% for $\mu_0 = 1000 \text{ km}^{-1}$ and 2.25% for $\mu_0 = 100 \text{ km}^{-1}$.

we resolve spatial scales of order μ_0^{-1} and show that our conclusions are not affected.

To quantify the differences between the cases with different resolution in Fig. 9, we compute the relative error by coarse-graining the results with 1500 radial bins and averaging over batches of 10 radial bins to compare the results with the ones from the numerical simulation with 150 radial bins. At each radius, the error is defined as relative error between the angle averaged population densities. We further average the relative error over all the radial bins to calculate the average relative error (see Ref. [52] for additional details). The average relative error at $t = 5 \times 10^{-5} \text{ s}$ between the two simulations with different number of radial bins is 1.16% for $\mu_0 = 1000 \text{ km}^{-1}$ and

2.25% for $\mu_0 = 100 \text{ km}^{-1}$. The figures demonstrate that the eventual existence of structures at small length scales of size μ_0^{-1} does not affect the results qualitatively even if the spatial resolution is not of that order. These findings are also in agreement with the ones presented in Refs. [38,47,84]. Figure 10 shows $|\rho_{xx}^{\text{mix}}/(\rho_{ee}^{\text{mix}} + \rho_{xx}^{\text{mix}})|$ for Cases A, B, and C using the default value of $\mu_0 = 10^4 \text{ km}^{-1}$ for the sake of completeness. In addition, Fig. 11 shows the same quantity for lower value of μ_0 for Case A (see also Fig. 9). Note that some of these plots should be interpreted with caution because of numerical artifacts in the top-left region where the denominator is very small.

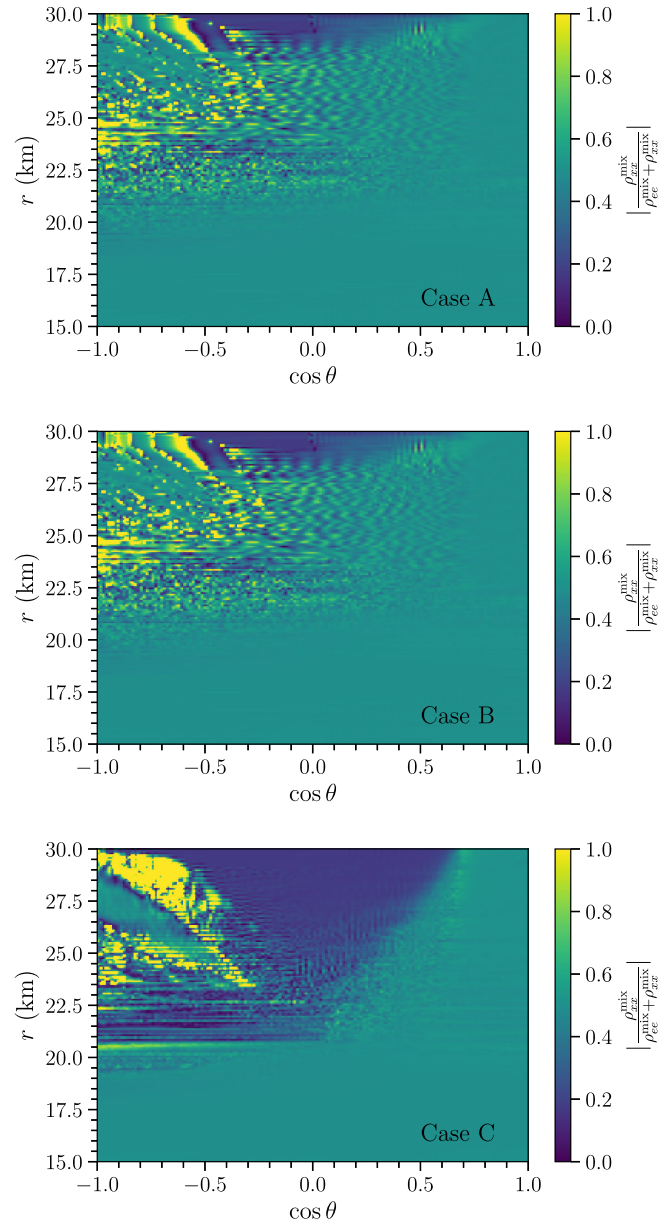


FIG. 10. Heatmap of $\left| \frac{\rho_{xx}^{\text{mix}}}{\rho_{ee}^{\text{mix}} + \rho_{xx}^{\text{mix}}} \right|$ after flavor conversion in the plane spanned by $\cos \theta$ and r for Cases A, B, and C for the default value of $\mu_0 = 10^4 \text{ km}^{-1}$.

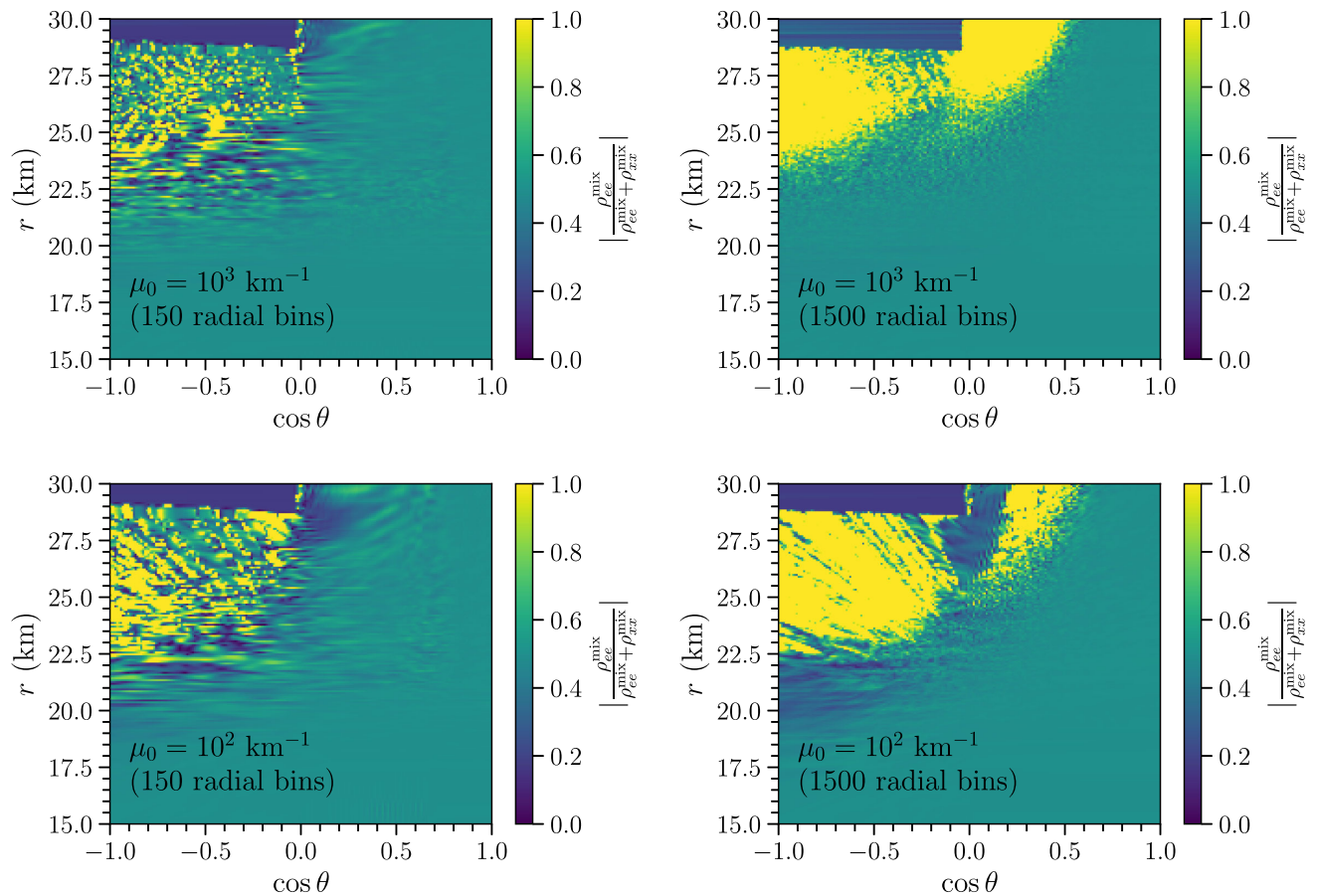


FIG. 11. Heatmap of $|\rho_{xx}^{\text{mix}}/(\rho_{ee}^{\text{mix}} + \rho_{xx}^{\text{mix}})|$ after flavor conversion in the plane spanned by $\cos \theta$ and r for Cases A for $\mu_0 = 10^3 \text{ km}^{-1}$ (top panels) and $\mu_0 = 10^2 \text{ km}^{-1}$ (bottom panels). The panels on the left have been obtained using 150 radial bins and the right panels have been obtained using 1500 radial bins. Note that the blue band in the top-left region is a numerical artifact, where the denominator is very small.

-
- [1] Adam Burrows and David Vartanian, Core-collapse supernova explosion theory, *Nature (London)* **589**, 29 (2021).
- [2] Hans-Thomas Janka, Tobias Melson, and Alexander Summa, Physics of core-collapse supernovae in three dimensions: A sneak preview, *Annu. Rev. Nucl. Part. Sci.* **66**, 341 (2016).
- [3] Hans A. Bethe and James R. Wilson, Revival of a stalled supernova shock by neutrino heating, *Astrophys. J.* **295**, 14 (1985).
- [4] Stirling A. Colgate and Richard H. White, The hydrodynamic behavior of supernovae explosions, *Astrophys. J.* **143**, 626 (1966).
- [5] James R. Wilson, Supernovae and post-collapse behavior, in *Numerical Astrophysics* (Jones and Bartlett, Boston, 1985), p. 422.
- [6] Stanislav P. Mikheyev and Alexei Yu. Smirnov, Resonance enhancement of oscillations in matter and solar neutrino spectroscopy, *Yad. Fiz.* **42**, 1441 (1985).
- [7] Lincoln Wolfenstein, Neutrino oscillations in matter, *Phys. Rev. D* **17**, 2369 (1978).
- [8] James T. Pantaleone, Neutrino oscillations at high densities, *Phys. Lett. B* **287**, 128 (1992).
- [9] Günther Sigl and Georg G. Raffelt, General kinetic description of relativistic mixed neutrinos, *Nucl. Phys.* **B406**, 423 (1993).
- [10] Huaiyu Duan, George M. Fuller, and Yong-Zhong Qian, Collective neutrino oscillations, *Annu. Rev. Nucl. Part. Sci.* **60**, 569 (2010).
- [11] Alessandro Mirizzi, Irene Tamborra, Hans-Thomas Janka, Ninetta Saviano, Kate Scholberg, Robert Bollig, Lorenz Hübepohl, and Sovan Chakraborty, Supernova

- neutrinos: Production, oscillations and detection, *Riv. Nuovo Cimento* **39**, 1 (2016).
- [12] Irene Tamborra and Shashank Shalgar, New developments in flavor evolution of a dense neutrino gas, *Annu. Rev. Nucl. Part. Sci.* **71**, 165 (2021).
- [13] Huaiyu Duan, George M. Fuller, J. Carlson, and Yong-Zhong Qian, Neutrino Mass Hierarchy and Stepwise Spectral Swapping of Supernova Neutrino Flavors, *Phys. Rev. Lett.* **99**, 241802 (2007).
- [14] Huaiyu Duan, George M. Fuller, J. Carlson, and Yong-Zhong Qian, Coherent Development of Neutrino Flavor in the Supernova Environment, *Phys. Rev. Lett.* **97**, 241101 (2006).
- [15] Huaiyu Duan, George M. Fuller, J. Carlson, and Yong-Zhong Qian, Simulation of coherent non-linear neutrino flavor transformation in the supernova environment. 1. Correlated neutrino trajectories, *Phys. Rev. D* **74**, 105014 (2006).
- [16] Huaiyu Duan, George M. Fuller, and Yong-Zhong Qian, Collective neutrino flavor transformation in supernovae, *Phys. Rev. D* **74**, 123004 (2006).
- [17] Gianluigi Fogli, Eligio Lisi, Antonio Marrone, and Alessandro Mirizzi, Collective neutrino flavor transitions in supernovae and the role of trajectory averaging, *J. Cosmol. Astropart. Phys.* **12** (2007) 010.
- [18] Gianluigi Fogli, Eligio Lisi, Antonio Marrone, Alessandro Mirizzi, and Irene Tamborra, Low-energy spectral features of supernova (anti)neutrinos in inverted hierarchy, *Phys. Rev. D* **78**, 097301 (2008).
- [19] Georg G. Raffelt and Alexei Yu. Smirnov, Self-induced spectral splits in supernova neutrino fluxes, *Phys. Rev. D* **76**, 081301 (2007); **77**, 029903(E) (2008).
- [20] Steen Hannestad, Georg G. Raffelt, Gunter Sigl, and Yvonne Y. Y. Wong, Self-induced conversion in dense neutrino gases: Pendulum in flavour space, *Phys. Rev. D* **74**, 105010 (2006); **76**, 029901(E) (2007).
- [21] Basudeb Dasgupta, Amol Dighe, Georg G. Raffelt, and Alexei Yu. Smirnov, Multiple Spectral Splits of Supernova Neutrinos, *Phys. Rev. Lett.* **103**, 051105 (2009).
- [22] Gianluigi Fogli, Eligio Lisi, Antonio Marrone, and Irene Tamborra, Supernova neutrinos and antineutrinos: Ternary luminosity diagram and spectral split patterns, *J. Cosmol. Astropart. Phys.* **10** (2009) 002.
- [23] Basudeb Dasgupta, Alessandro Mirizzi, Irene Tamborra, and Ricard Tomas, Neutrino mass hierarchy and three-flavor spectral splits of supernova neutrinos, *Phys. Rev. D* **81**, 093008 (2010).
- [24] Alexander Friedland, Self-Refraction of Supernova Neutrinos: Mixed Spectra and Three-Flavor Instabilities, *Phys. Rev. Lett.* **104**, 191102 (2010).
- [25] Georg G. Raffelt, Srdjan Sarikas, and David de Sousa Seixas, Axial Symmetry Breaking in Self-Induced Flavor Conversion of Supernova Neutrino Fluxes, *Phys. Rev. Lett.* **111**, 091101 (2013); **113**, 239903(E) (2014).
- [26] Huaiyu Duan and Shashank Shalgar, Flavor instabilities in the neutrino line model, *Phys. Lett. B* **747**, 139 (2015).
- [27] Shashank Shalgar and Irene Tamborra, On the occurrence of crossings between the angular distributions of electron neutrinos and antineutrinos in the supernova core, *Astrophys. J.* **883**, 80 (2019).
- [28] Hiroki Nagakura, Lucas Johns, Adam Burrows, and George M. Fuller, Where, when, and why: Occurrence of fast-pairwise collective neutrino oscillation in three-dimensional core-collapse supernova models, *Phys. Rev. D* **104**, 083025 (2021).
- [29] Raymond F. Sawyer, Speed-up of neutrino transformations in a supernova environment, *Phys. Rev. D* **72**, 045003 (2005).
- [30] Raymond F. Sawyer, The multi-angle instability in dense neutrino systems, *Phys. Rev. D* **79**, 105003 (2009).
- [31] Raymond F. Sawyer, Neutrino Cloud Instabilities Just Above the Neutrino Sphere of a Supernova, *Phys. Rev. Lett.* **116**, 081101 (2016).
- [32] Sovan Chakraborty, Rasmus Hansen, Ignacio Izaguirre, and Georg G. Raffelt, Collective neutrino flavor conversion: Recent developments, *Nucl. Phys.* **B908**, 366 (2016).
- [33] Sovan Chakraborty, Rasmus Sloth Hansen, Ignacio Izaguirre, and Georg G. Raffelt, Self-induced neutrino flavor conversion without flavor mixing, *J. Cosmol. Astropart. Phys.* **03** (2016) 042.
- [34] Ignacio Izaguirre, Georg G. Raffelt, and Irene Tamborra, Fast Pairwise Conversion of Supernova Neutrinos: A Dispersion-Relation Approach, *Phys. Rev. Lett.* **118**, 021101 (2017).
- [35] Changhao Yi, Lei Ma, Joshua D. Martin, and Huaiyu Duan, Dispersion relation of the fast neutrino oscillation wave, *Phys. Rev. D* **99**, 063005 (2019).
- [36] Joshua D. Martin, Changhao Yi, and Huaiyu Duan, Dynamic fast flavor oscillation waves in dense neutrino gases, *Phys. Lett. B* **800**, 135088 (2020).
- [37] Shashank Shalgar and Irene Tamborra, Dispelling a myth on dense neutrino media: Fast pairwise conversions depend on energy, *J. Cosmol. Astropart. Phys.* **01** (2021) 014.
- [38] Shashank Shalgar, Ian Padilla-Gay, and Irene Tamborra, Neutrino propagation hinders fast pairwise flavor conversions, *J. Cosmol. Astropart. Phys.* **06** (2020) 048.
- [39] Shashank Shalgar and Irene Tamborra, Three flavor revolution in fast pairwise neutrino conversion, *Phys. Rev. D* **104**, 023011 (2021).
- [40] Lucas Johns, Hiroki Nagakura, George M. Fuller, and Adam Burrows, Neutrino oscillations in supernovae: Angular moments and fast instabilities, *Phys. Rev. D* **101**, 043009 (2020).
- [41] Madhurima Chakraborty and Sovan Chakraborty, Three flavor neutrino conversions in supernovae: Slow & fast instabilities, *J. Cosmol. Astropart. Phys.* **01** (2020) 005.
- [42] Sajad Abbar, Huaiyu Duan, Kohsuke Sumiyoshi, Tomoya Takiwaki, and Maria Cristina Volpe, On the occurrence of fast neutrino flavor conversions in multidimensional supernova models, *Phys. Rev. D* **100**, 043004 (2019).
- [43] Basudeb Dasgupta, Alessandro Mirizzi, and Manibrata Sen, Fast neutrino flavor conversions near the supernova core with realistic flavor-dependent angular distributions, *J. Cosmol. Astropart. Phys.* **02** (2017) 019.
- [44] Francesco Capozzi, Madhurima Chakraborty, Sovan Chakraborty, and Manibrata Sen, Fast Flavor Conversions in Supernovae: The Rise of Mu-Tau Neutrinos, *Phys. Rev. Lett.* **125**, 251801 (2020).
- [45] Francesco Capozzi, Madhurima Chakraborty, Sovan Chakraborty, and Manibrata Sen, Supernova fast flavor

- conversions in $1 + 1D$: Influence of mu-tau neutrinos, *Phys. Rev. D* **106**, 083011 (2022).
- [46] Shashank Shalgar and Irene Tamborra, Symmetry breaking induced by pairwise conversion of neutrinos in compact sources, *Phys. Rev. D* **105**, 043018 (2022).
- [47] Shashank Shalgar and Irene Tamborra, A change of direction in pairwise neutrino conversion physics: The effect of collisions, *Phys. Rev. D* **103**, 063002 (2021).
- [48] Lucas Johns, Collisional flavor instabilities of supernova neutrinos, [arXiv:2104.11369](https://arxiv.org/abs/2104.11369).
- [49] Rasmus S.L. Hansen, Shashank Shalgar, and Irene Tamborra, Enhancement or damping of fast neutrino flavor conversions due to collisions, *Phys. Rev. D* **105**, 123003 (2022).
- [50] Lucas Johns and Hiroki Nagakura, Self-consistency in models of neutrino scattering and fast flavor conversion, *Phys. Rev. D* **106**, 043031 (2022).
- [51] Joshua D. Martin, J. Carlson, Vincenzo Cirigliano, and Huaiyu Duan, Fast flavor oscillations in dense neutrino media with collisions, *Phys. Rev. D* **103**, 063001 (2021).
- [52] Shashank Shalgar and Irene Tamborra, Supernova neutrino decoupling is altered by flavor conversion, [arXiv:2206.00676](https://arxiv.org/abs/2206.00676).
- [53] Sherwood Richers, Donald Willcox, and Nicole Ford, Neutrino fast flavor instability in three dimensions, *Phys. Rev. D* **104**, 103023 (2021).
- [54] Hiroki Nagakura and Masamichi Zaizen, Time-Dependent, Quasi-Steady, and Global Features of Fast Neutrino-Flavor Conversion, *Phys. Rev. Lett.* **129**, 261101 (2022).
- [55] Zewei Xiong, Andre Sieverding, Manibrata Sen, and Yong-Zhong Qian, Potential impact of fast flavor oscillations on neutrino-driven winds and their nucleosynthesis, *Astrophys. J.* **900**, 144 (2020).
- [56] Meng-Ru Wu, Irene Tamborra, Oliver Just, and Hans-Thomas Janka, Imprints of neutrino-pair flavor conversions on nucleosynthesis in ejecta from neutron-star merger remnants, *Phys. Rev. D* **96**, 123015 (2017).
- [57] Oliver Just, Sajad Abbar, Meng-Ru Wu, Irene Tamborra, Hans-Thomas Janka, and Francesco Capozzi, Fast neutrino conversion in hydrodynamic simulations of neutrino-cooled accretion disks, *Phys. Rev. D* **105**, 083024 (2022).
- [58] Manu George, Meng-Ru Wu, Irene Tamborra, Ricard Ardevol-Pulpillo, and Hans-Thomas Janka, Fast neutrino flavor conversion, ejecta properties, and nucleosynthesis in newly-formed hypermassive remnants of neutron-star mergers, *Phys. Rev. D* **102**, 103015 (2020).
- [59] Xinyu Li and Daniel M. Siegel, Neutrino Fast Flavor Conversions in Neutron-Star Postmerger Accretion Disks, *Phys. Rev. Lett.* **126**, 251101 (2021).
- [60] Irene Tamborra, Lorenz Hüdepohl, Georg G. Raffelt, and Hans-Thomas Janka, Flavor-dependent neutrino angular distribution in core-collapse supernovae, *Astrophys. J.* **839**, 132 (2017).
- [61] Milad Delfan Azari, Shoichi Yamada, Taiki Morinaga, Wakana Iwakami, Hirotada Okawa, Hiroki Nagakura, and Kohsuke Sumiyoshi, Linear analysis of fast-pairwise collective neutrino oscillations in core-collapse supernovae based on the results of Boltzmann simulations, *Phys. Rev. D* **99**, 103011 (2019).
- [62] Milad Delfan Azari, Shoichi Yamada, Taiki Morinaga, Hiroki Nagakura, Shun Furusawa, Akira Harada, Hirotada Okawa, Wakana Iwakami, and Kohsuke Sumiyoshi, Fast collective neutrino oscillations inside the neutrino sphere in core-collapse supernovae, *Phys. Rev. D* **101**, 023018 (2020).
- [63] Milad Delfan Azari, Shoichi Yamada, Taiki Morinaga, Wakana Iwakami, Hirotada Okawa, Hiroki Nagakura, and Kohsuke Sumiyoshi, Linear analysis of fast-pairwise collective neutrino oscillations in core-collapse supernovae based on the results of Boltzmann simulations, *Phys. Rev. D* **99**, 103011 (2019).
- [64] Taiki Morinaga, Hiroki Nagakura, Chinami Kato, and Shoichi Yamada, Fast neutrino-flavor conversion in the preshock region of core-collapse supernovae, *Phys. Rev. Res.* **2**, 012046 (2020).
- [65] Robert Glas, Hans-Thomas Janka, Francesco Capozzi, Manibrata Sen, Basudeb Dasgupta, Alessandro Mirizzi, and Guenter Sigl, Fast Neutrino flavor instability in the neutron-star convection layer of three-dimensional supernova models, *Phys. Rev. D* **101**, 063001 (2020).
- [66] Sajad Abbar, Huaiyu Duan, Kohsuke Sumiyoshi, Tomoya Takiwaki, and Maria Cristina Volpe, Fast neutrino flavor conversion modes in multidimensional core-collapse supernova models: The role of the asymmetric neutrino distributions, *Phys. Rev. D* **101**, 043016 (2020).
- [67] Hiroki Nagakura, Taiki Morinaga, Chinami Kato, and Shoichi Yamada, Fast-pairwise collective neutrino oscillations associated with asymmetric neutrino emissions in core-collapse supernovae, *Astrophys. J.* **886**, 139 (2019).
- [68] Sajad Abbar, Francesco Capozzi, Robert Glas, H. Thomas Janka, and Irene Tamborra, On the characteristics of fast neutrino flavor instabilities in three-dimensional core-collapse supernova models, *Phys. Rev. D* **103**, 063033 (2021).
- [69] Francesco Capozzi, Sajad Abbar, Robert Bollig, and Hans-Thomas Janka, Fast neutrino flavor conversions in one-dimensional core-collapse supernova models with and without muon creation, *Phys. Rev. D* **103**, 063013 (2021).
- [70] Akira Harada and Hiroki Nagakura, Prospects of fast flavor neutrino conversion in rotating core-collapse supernovae, *Astrophys. J.* **924**, 109 (2022).
- [71] G. Sigl and G.G. Raffelt, General kinetic description of relativistic mixed neutrinos, *Nucl. Phys.* **B406**, 423 (1993).
- [72] Markus Rapp and H. Thomas Janka, Radiation hydrodynamics with neutrinos: Variable Eddington factor method for core collapse supernova simulations, *Astron. Astrophys.* **396**, 361 (2002).
- [73] A. Esteban-Pretel, A. Mirizzi, S. Pastor, R. Tomas, G. G. Raffelt, P. D. Serpico, and G. Sigl, Role of dense matter in collective supernova neutrino transformations, *Phys. Rev. D* **78**, 085012 (2008).
- [74] Steven Weinberg, *Lectures on Astrophysics* (Cambridge University Press, Cambridge, England, 2019).
- [75] R.L. Bowers and J.R. Wilson, A numerical model for stellar core collapse calculations, *Astrophys. J. Suppl. Ser.* **50**, 115 (1982).
- [76] Evan O'Connor, An open-source neutrino radiation hydrodynamics code for core-collapse supernovae, *Astrophys. J. Suppl. Ser.* **219**, 24 (2015).

- [77] Anthony Mezzacappa, Eirik Endeve, O. E. Bronson Messer, and Stephen W. Bruenn, Physical, numerical, and computational challenges of modeling neutrino transport in core-collapse supernovae, *Liv. Rev. Comput. Astrophys.* **6**, 4 (2020).
- [78] Sherwood A. Richers, Gail C. McLaughlin, James P. Kneller, and Alexey Vlasenko, Neutrino quantum kinetics in compact objects, *Phys. Rev. D* **99**, 123014 (2019).
- [79] S. W. Bruenn, Stellar core collapse—Numerical model and infall epoch, *Astrophys. J. Suppl. Ser.* **58**, 771 (1985).
- [80] G. G. Raffelt, *Stars as Laboratories for Fundamental Physics: The Astrophysics of Neutrinos, Axions, and Other Weakly Interacting Particles* (The university of Chicago press, Chicago, 1996).
- [81] Christopher Rackauckas and Qing Nie, Differentialequations.JL-A performant and feature-rich ecosystem for solving differential equations in Julia, *J. Open Res. Software* **5**, 15 (2017).
- [82] Jeff Bezanson, Alan Edelman, Stefan Karpinski, and Viral B. Shah, Julia: A fresh approach to numerical computing, *SIAM Rev.* **59**, 65 (2017).
- [83] Taiki Morinaga, Fast neutrino flavor instability and neutrino flavor lepton number crossings, *Phys. Rev. D* **105**, L101301 (2022).
- [84] Ian Padilla-Gay, Shashank Shalgar, and Irene Tamborra, Multi-dimensional solution of fast neutrino conversions in binary neutron star merger remnants, *J. Cosmol. Astropart. Phys.* **01** (2021) 017.
- [85] Arka Banerjee, Amol Dighe, and Georg G. Raffelt, Linearized flavor-stability analysis of dense neutrino streams, *Phys. Rev. D* **84**, 053013 (2011).
- [86] Georg G. Raffelt and Alexei Yu. Smirnov, Adiabaticity and spectral splits in collective neutrino transformations, *Phys. Rev. D* **76**, 125008 (2007).
- [87] Alessandro Mirizzi and Pasquale D. Serpico, Instability in the Dense Supernova Neutrino Gas with Flavor-Dependent Angular Distributions, *Phys. Rev. Lett.* **108**, 231102 (2012).
- [88] Alessandro Mirizzi and Pasquale Dario Serpico, Flavor stability analysis of dense supernova neutrinos with flavor-dependent angular distributions, *Phys. Rev. D* **86**, 085010 (2012).
- [89] Ian Padilla-Gay, Irene Tamborra, and Georg G. Raffelt, Neutrino Flavor Pendulum Reloaded: The Case of Fast Pairwise Conversion, *Phys. Rev. Lett.* **128**, 121102 (2022).
- [90] Lucas Johns, Hiroki Nagakura, George M. Fuller, and Adam Burrows, Fast oscillations, collisionless relaxation, and spurious evolution of supernova neutrino flavor, *Phys. Rev. D* **102**, 103017 (2020).
- [91] Meng-Ru Wu, Manu George, Chun-Yu Lin, and Zewei Xiong, Collective fast neutrino flavor conversions in a 1D box: Initial conditions and long-term evolution, *Phys. Rev. D* **104**, 103003 (2021).
- [92] Sherwood Richers, Don E. Willcox, Nicole M. Ford, and Andrew Myers, Particle-in-cell simulation of the neutrino fast flavor instability, *Phys. Rev. D* **103**, 083013 (2021).
- [93] Soumya Bhattacharyya and Basudeb Dasgupta, Fast Flavor Depolarization of Supernova Neutrinos, *Phys. Rev. Lett.* **126**, 061302 (2021).